Interfacial energy constraints are sufficient to align cells over large distances

S. Tlili[1], M. Shagirov[1], S. Zhang[1] and T. E. Saunders[1,2,3,#]

[1] Mechanobiology Institute, National University of Singapore, Singapore
[2] Department of Biological Sciences, National University of Singapore, Singapore
[3] Institute of Molecular and Cell Biology, A*Star, Singapore
[#] Correspondence: dbsste@nus.edu.sg

During development and wound healing, cells need to form long-ranged ordered structures to ensure precise formation of organs and repair damage. This requires cells to locate specific partner cells to which to adhere. How such cell matching reliably happens is an open problem, particularly in the presence of biological variability. Here, we use an equilibrium energy model to simulate how cell matching can occur with subcellular precision. A single parameter – encapsulating the competition between selective cell adhesion and cell elasticity – can reproduce experimental observations of cell alignment in the *Drosophila* embryonic heart. This demonstrates that adhesive differences between cells (in the case of the heart, mediated by filopodia interactions) are sufficient to drive cell matching without requiring cell rearrangements. The model can explain observed matching defects in mutant conditions and when there is significant biological variability. We also demonstrate that a dynamic vertex model gives results consistent with the equilibrium energy model. Overall, this work shows that equilibrium energy considerations are consistent with observed cell matching in cardioblasts, and has potential application to other systems, such as neuron connections and wound repair.

Introduction

During development, cells interact collectively to form tissues and organs through a series of morphological transformations, driven by cell proliferation, rearrangements, migration and death[1-4]. When these processes fail, the final shape of the tissue can be defective, resulting in diseases, including cardiomyopathies[5] and neurological defects[6,7]. During organogenesis, cells often need to identify specific cells to which to adhere. A classic example is formation of human facial structures[6]; cells initially undergo long-ranged migration from distinct regions of the neural plate before forming precise connections to create structures such as the lip. Errors in this process lead to birth defects such as cleft lip and facial cleft[7]. During neurogenesis, neurons also need to form precise linkages to their synaptic partners[8-10] with severe consequences if these processes fail. A range of molecules have been identified that are involved in cell matching, predominantly from neuronal systems[11-14]. These molecules include cytoskeletal, adhesion, and force transducing proteins. However, the underlying mechanisms by which the information from these different components is integrated by the developing tissue to form precise connections remain unknown.

In most tissues, there are multiple cell types with stereotypic spatial positions. For example, formation of the eye requires precise cell fate determination and positioning[15,16], even within a growing domain[17]. In the developing heart, cardioblasts take on different fates depending on expression of (highly conserved) transcription factors[18]. Periodic patterns of cells can also be generated from lateral inhibition[19,20]. Such periodic patterns need to be maintained across large distances, even as tissues undergo large-scale morphological changes.

Theoretical modelling of tissue formation has helped increase our understanding of how cells pack[21], form compartment boundaries[22], generate complex tissue shapes[23-26], and ensure regulated growth[27]. Lateral inhibition can create a wide variety of patterns depending on the feedback mechanisms[28]. Recently, vertex models have been used to understand cell structure in epithelia[29,30]. Although biological systems are inherently dynamic, equilibrium statistical mechanics can be a powerful tool for understanding suitable biological processes. An example of such a case is cell packing in the eye, where analogies with soap bubbles provide an effective tool for understanding formation of the *Drosophila* retina[31].

Here, we develop a model of cell matching where differential adhesion energy constraints between cells drives the process of matching. We apply this to the developing *Drosophila* embryonic heart, where the process of cardioblast cell matching has recently been quantified[32]. The *Drosophila* embryonic heart is comprised of two lines of cardioblasts that migrate together over a period of a few hours, Figure 1A, and they express either Tinman (Tin, the *Drosophila* homolog of mammalian Nkx2.5) or Seven-up (Svp), Figure 1B, in a repeating 4-2 pattern[33]. As cardioblasts approach each other, the cells adjust position, via filopodia interactions between cardioblasts, to align accurately with their contralateral partners, Figure 1C-D. Specific adhesion molecules are expressed within the different cardioblast types: Fasciclin III (Fas3) in Tin-positive cardioblasts; and Ten-m in Svp-positive cardioblasts, Figure 1E. Cell matching in the heart, as defined in Figure 2A, depends on the differential spatial expression of these adhesion molecules[32], Figure 2B-C. Motivated by these observations, we construct a biophysical model of the cell-cell interactions to test whether such differential adhesion is sufficient to drive cell matching. We then use this model to test how both structural and genetic perturbations alter cell matching. This model provides a biophysical framework in which to understand how cells find specific partners during development.

Results

Mapping of adhesive interactions between filopodia onto an equilibrium energy state

To simulate cell matching, we developed an energy-based model that accounts for the spatial constraints between cells and the adhesion competition between different cell types. In the *Drosophila* heart, differential adhesion between cells is mediated by filopodia contacts, which have a spread of contact times[32], from a few seconds to over five minutes. As justified below, the underlying principle of the model is that these differential filopodia adhesion times between adhering cells can be mapped onto effective adhesion energies.

At a biochemical level, the time for reactions, τ, are typically related to the Arhennius law: $\tau \sim \tau_0 e^{\Delta E/k_B T}$, where ΔE is the energy cost of the reaction. It has recently been shown that time scales in biological systems at macroscopic levels can also follow the Arhennius law, such as in the developmental time of *Drosophila* embryogenesis[34,35]. Here, we apply a *mesoscopic* approximation, where we assume that the distribution of binding times of filopodia τ_{bind} can be related to the effective adhesion energy barrier ΔE_{adh} to separate contacting filopodia.

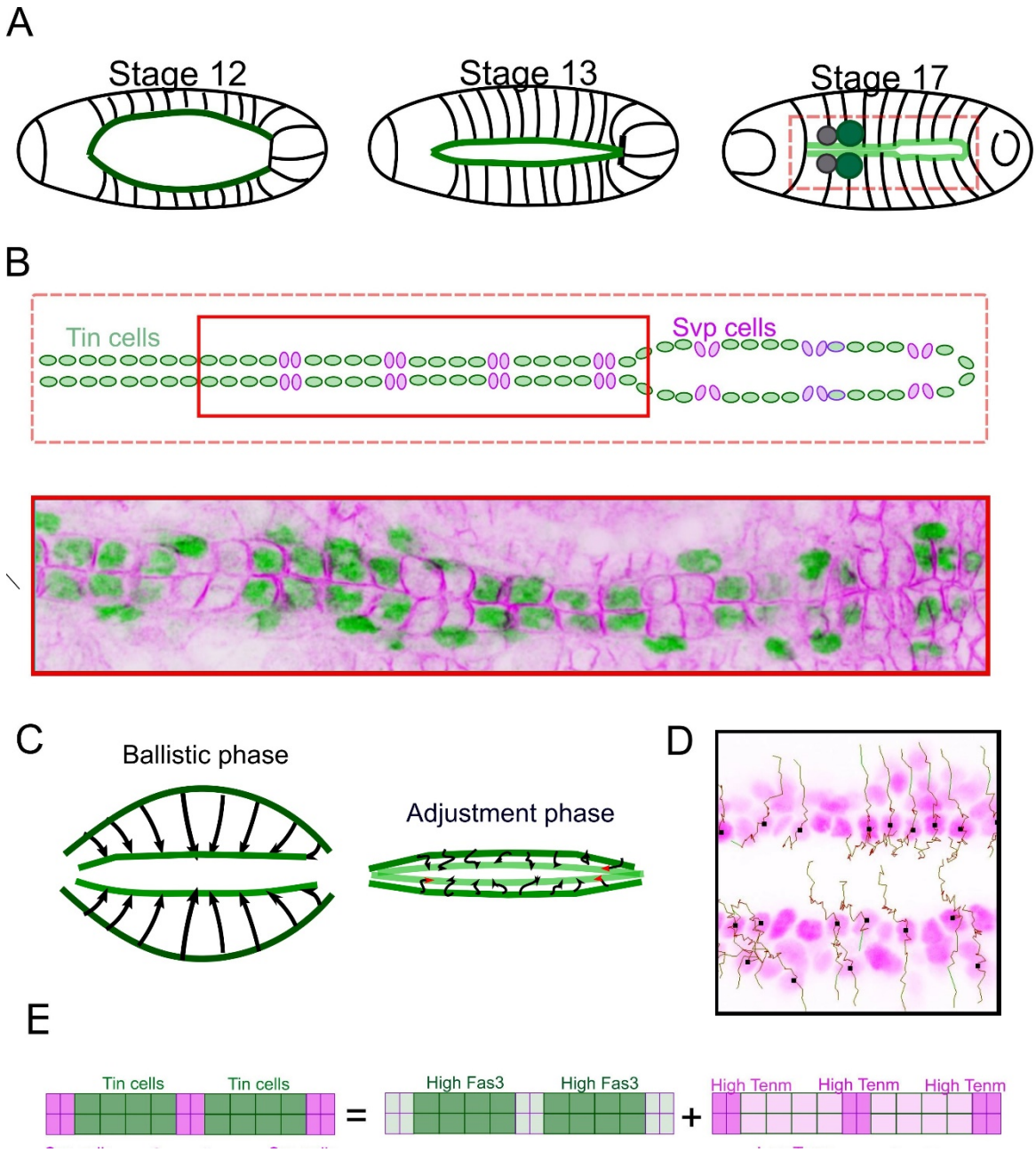

Figure 1. **Cell matching in *Drosophila* embryonic heart.** (A) Developmental stages of heart formation. Cardioblasts (green regions) merge to form a tubular heart. (B) Cardioblasts have distinct expression patterns. Heart structure at larval stage: the heart is made of a periodic alternation of Tin cells and Svp cells. Staining of cardioblasts (Spectrin in magenta and Tinman in green). (C) Heart formation is initially driven by global tissue movement during dorsal closure but active processes align cells in a final adjustment phase. (D) Example of cell trajectories during the adjustment phase. (E) Cardioblasts express the adhesion molecules Fas3 and Ten-m in an alternating pattern.

In the model, the overlap between facing cells results in an adhesion energy $\Delta E = -\epsilon . x$, where x denotes the length of the cell contact interface and ϵ is the adhesion energy per unit length between the two cells, Figure 2D. Cellular compressibility for each cell is encoded by an effective elastic energy $E_{el} = K(L_{cell} - L_0)^2$, corresponding to the cost of deforming the cells away from their preferred cross-sectional width; K is the effective cell compressibility along its leading edge, L_{cell} the cell length and L_0 the cell rest length, Figure 2D. We only focus on the apical leading edge of the cells as this is where the process of cell alignment is occurring. Combining the energy scales, we can express effective energies for two cell types, denoted by a and b:

$$E_a = K\left(L_{cell} - L_{0,a}\right)^2 - (\epsilon_{aa} . x + \epsilon_{ab} . y) \quad (1)$$

$$E_b = K\left(L_{cell} - L_{0,b}\right)^2 - (\epsilon_{bb} . x + \epsilon_{ab} . y) \quad (2)$$

ϵ_{ab} denotes the adhesion energy per unit length between cells of type a and b, x and y denote the total alignment overlap with cells of the same and different types respectively, and $L_{0,a}$ and $L_{0,b}$ represent the equilibrium lengths for the different cell types.

Filopodia activity results from the interplay between active fluctuations and adhesion interactions with other filopodia. The active alignment of the heart takes place over a period of around 30 minutes, whereas the average binding time of filopodia is 1-5 minutes. In the following, we assume that the heart has enough time during the active alignment process to reach equilibrium.

To simulate the evolution and equilibration of configurations of heart cell, we use a Metropolis algorithm incorporating mechanical fluctuations induced by filopodia activity as an effective temperature, see Figure 2E and Methods for further details. We define cellular mismatch by identifying the fraction of cell boundaries that are not correctly aligned with their corresponding opposite cell, Figure 2A. In this definition, a perfectly aligned tissue has mismatch of 0, while a fully misaligned system has a mismatch of 1. The tissue mismatch is then taken as the average over all cell mismatches.

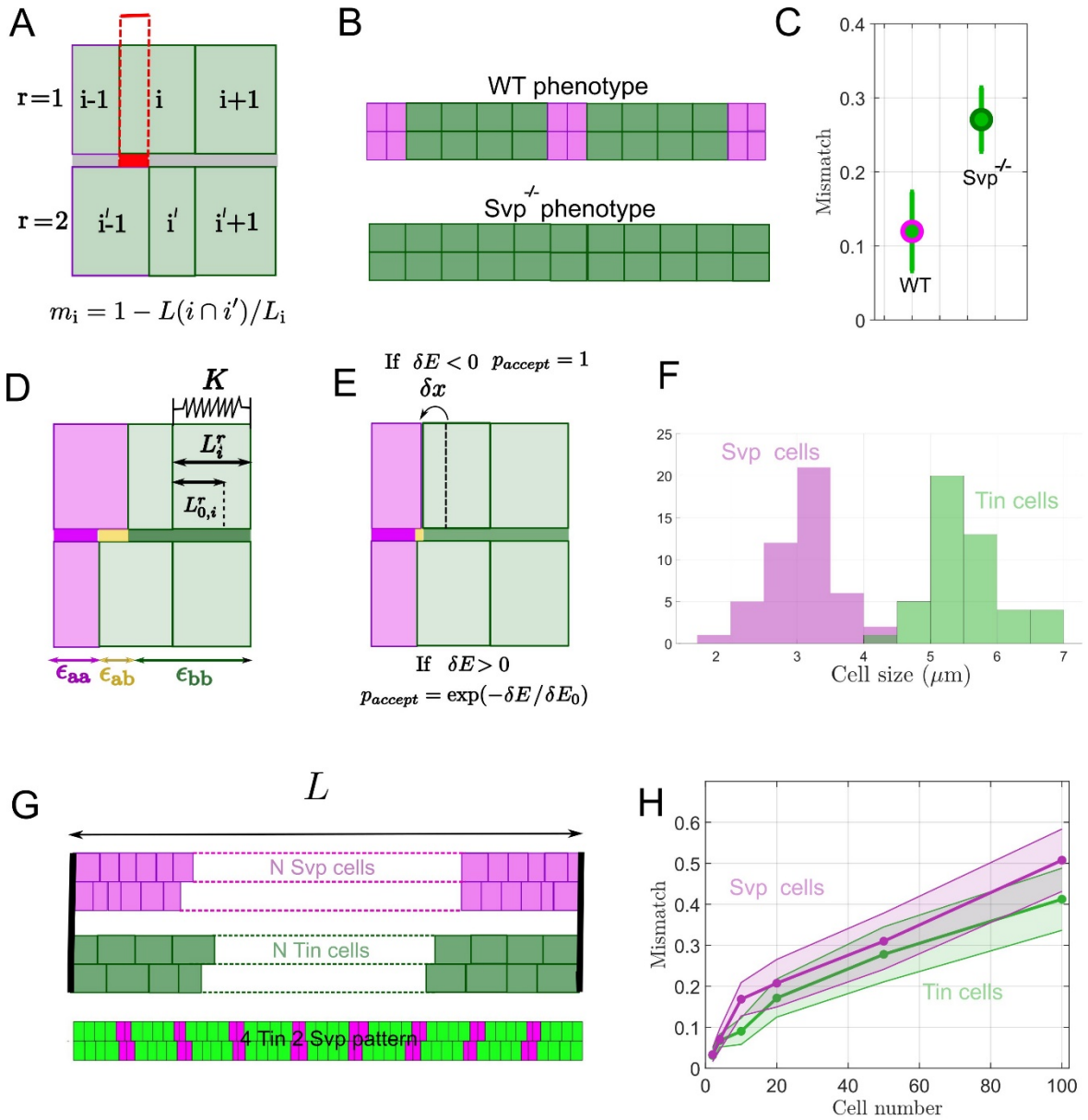

Figure 2: **Simulating heart matching** (A) Definition of cell mismatch. *r=1,2* denotes two contralateral rows of cardioblasts. (B,C) When different cell types are not present (as in *svp*$^{-/-}$), the resulting heart has severe mismatching defects. (D) Cells can deform elastically from their rest length with a compressibility K and cell-cell contact is characterized by an adhesion depending of the contact type. (E) Metropolis algorithm is used to find the final cell alignment after equilibration. At each step, a cell/cell interface is randomly chosen and is displaced by δx, which follows a Gaussian distribution (see Methods). The probability to accept the displacement follows the Metropolis algorithm (F) Distribution of leading edge size in different cardioblast types. (G) Simulations with only one cell type (all Svp or all Tin) and with the alternated pattern of Tin/Svp cells. (H) Predicted mismatch in hearts with one cell type for different cells number.

140 **Minimization of interfacial energy constraints are sufficient to explain cell alignment in**
141 **the wildtype *Drosophila* heart**
142 We apply our model to the developing *Drosophila* heart, where quantitative data for cell
143 matching is available[32]. As well as incorporating the effective energy differences, we need to
144 implement within the simulation a representative pattern of cell types. In the *Drosophila* heart,
145 Tin-positive cardioblasts express Fas3 at high levels and Svp-positive cardioblasts express
146 Ten-m. We translate this into different adhesion energies per unit length between Tin-positive
147 cardioblasts (ϵ_{TT}), Svp-positive cardioblasts (ϵ_{SS}), and between Tin- and Svp-positive
148 cardioblasts (ϵ_{ST}), similar to the outline given in Figure 1B-E.
149
150 *Initial configuration of the cells and initial cell alignment:* By the end of dorsal closure,
151 cardioblasts are brought into close contact. To initiate the cellular arrangement, we assume that
152 the cells at the two ends of the heart are perfectly aligned and are at their resting length initially.
153 To model geometric disorder, we take the length of the apical surfaces for Tin-positive and
154 Svp-positive cardioblasts as $L_{0,T}$ and $L_{0,S}$ respectively. These lengths are simulated as Gaussian
155 variables of mean $L_{0,T}^{mean}$ and $L_{0,S}^{mean}$ with standard deviation $L_{0,T}^{std}$ and $L_{0,S}^{std}$, extracted from
156 experimental quantification of cell size (Figure 2F). We construct the simulated heart as two
157 rows of cells formed by a succession of four Tin-positive cells and two Svp-positive cells
158 patterns, with a total number of N_1 =52 cells (number of cells in a heart row, Figure 1B and
159 2G). Each cell length is picked as a random variable according to the rest lengths distributions
160 (Figure 2F). However, we constrain the total lengths of the two rows to be identical (Methods).
161
162 *Initial cell matching without adhesion energy:* We first consider the question: are the boundary
163 constraints alone sufficient to ensure robust cell matching? To answer this, we take initial
164 conditions that mirror experimentally measured cardioblast size and position (Figure 2F-G) but
165 with no adhesion energy (*i.e.* $\epsilon_{TT} = \epsilon_{SS} = \epsilon_{ST} = 0$), Figure 2D. As we take cells at their initial
166 rest length, no equilibration is needed and we calculate the mismatch of the initial condition.
167 We simulate N_2 = 30 embryos with confinement of different sizes, and calculate the ensemble
168 mismatch in cell alignment. This results in a mismatch increasing with system size, Figure 2H.
169 Interestingly, we find for N_1 =52 cells (the experimental size of the heart) a mismatch around
170 0.3 which corresponds to the mismatch value experimentally observed in the *Svp*$^{-/-}$ mutants
171 where all cells are of the same type, Figure 2C. In summary, geometric disorder, induced by
172 cell size variability, is too large to enable precise cell matching merely by boundary constraints.

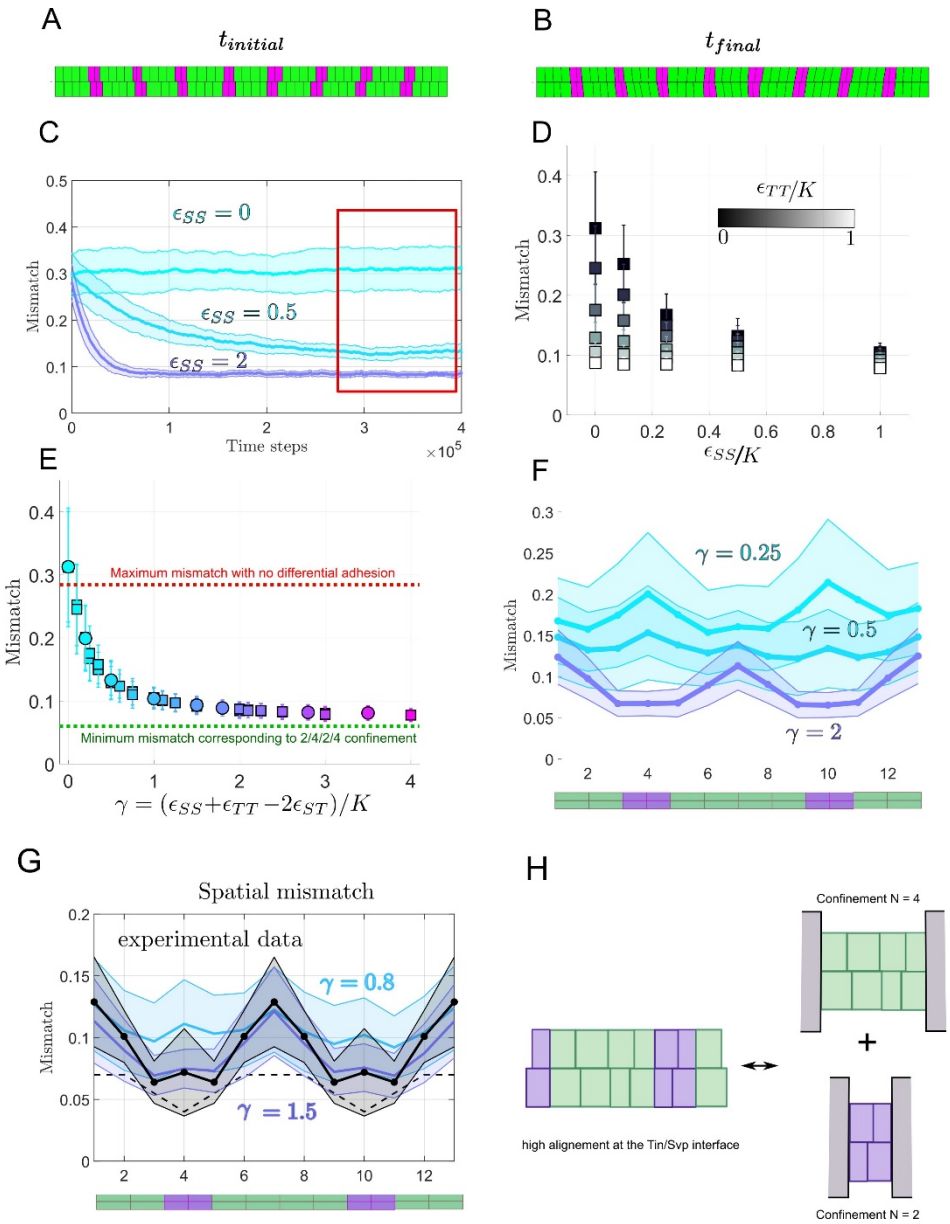

Figure 3: **The interplay between differential adhesion, cell compressibility and cell size variability determines the cell-matching.** (A) Initial configuration randomly sampled for 52 cells (4 Tin/2 Svp alternated pattern). (B) Cells configuration after convergence of mismatch, cell lengths have changed on the cell/cell interface while we still represent their initial length and position on the side not touching the interface. (C) Ensemble averaged (N_2 = 30 simulated embryos) mismatch evolution for different values of ε_{SS} and K = 1. All mismatches are calculated at steady state. (D) Final mismatch for different values of ε_{SS} and ε_{TT}. (E) Final mismatch for different values of γ. Circles correspond to the case $\varepsilon_{ST} = 0$ and squares to $\varepsilon_{ST} \neq 0$. (F) Spatial variation of mismatch across different cell types as depicted in the below cartoon (green = Tin positive cardioblasts, magenta = Svp positive cardioblasts.). (G) Spatial variations of the mismatch in the wildtype (in black) and comparison with the simulation (blue, purple). (H) Sketch showing how differential adhesion aligns heterogeneous cell-cell contacts, which generates local confinement of cells.

186 *Calculating the mismatch with differential cell adhesion:* We next investigate how the strength
187 of selective adhesion impacts alignment. We first explore matching variations with only one
188 cell type adhering, *i.e.* we vary ϵ_{SS} alone with $\epsilon_{TT} = 0$ $\epsilon_{ST} = 0$, Figure 3A-C. We compute
189 mismatch evolution of the embryo as a function of simulation iterations and take its value once
190 it reaches a steady-state value, Figure 3C. The final mismatch for a single embryo simulation
191 is averaged over 30 embryos. We find that the final mismatch decreases with increasing
192 adhesion level. We then explored two cell types with selective adhesion by using different
193 combinations of ϵ_{SS} and ϵ_{TT} with $\epsilon_{ST} = 0$, Figure 3D. Different combinations of ϵ_{SS} and ϵ_{TT}
194 can lead to the same alignment. By systematically varying ϵ_{SS}, ϵ_{TT} and ϵ_{ST}, we see that the
195 equilibrium mismatch is determined by the parameter $\gamma = \frac{(\epsilon_{TT}-\epsilon_{ST})+(\epsilon_{SS}-\epsilon_{ST})}{K}$, representing the
196 competition between cells due to differential adhesion and cell compressibility, Figure 3E.
197 Here, γ corresponds to the typical length change that adhesion differences can generate for a
198 single cell. For $\gamma = 0\mu m$, there is no energy cost for different cell types to have a contact
199 interface. The mismatch corresponds to the random case simulated in Figure 2H; similar to the
200 *Svp*$^{-/-}$ mutant, where all cells are of the same type. Mismatch decreases with increasing γ,
201 reaching a plateau around mismatch of ~ 0.07, dashed line in Figure 3E. This implies that,
202 beyond a certain level, increasing differential adhesion only weakly improves matching.
203
204 We measure spatial variations of the mismatch, denoted by *m*, Figure 3F. We find that *m* is
205 minimal at the Tin-Svp interface, as any contact between different cell types has some adhesion
206 energy cost for $\gamma > 0\mu m$, Figure 3G. Alignment of cells inside a block of homogeneous cell
207 types in the high γ limit is determined by the boundaries imposed by the highly aligned cells
208 at the interface between different cell types. Within a region of Tin-positive cells, the level of
209 cell mismatch converges towards the non-adhesive random case with N = 4, Figure 3H. The
210 mismatch between Svp-positive cells is similar to the random adhesion case with N = 2. The
211 geometric variability in the lengths of the cell leading edges means that cells never reach zero
212 mismatch even at very high adhesion values. Interestingly, for small values of γ, the pattern of
213 cell mismatch is inverted, as geometric variability is higher for Svp cells.
214
215 Comparing the spatial profile of cell matching to the experimental data, we see that for $\gamma >$
216 $1\mu m$ the mismatch profile agrees well with experiment, Figure 3G. Therefore, simple energy
217 considerations, with a single fitting parameter γ, are sufficient to reproduce the wildtype
218 matching phenotype.

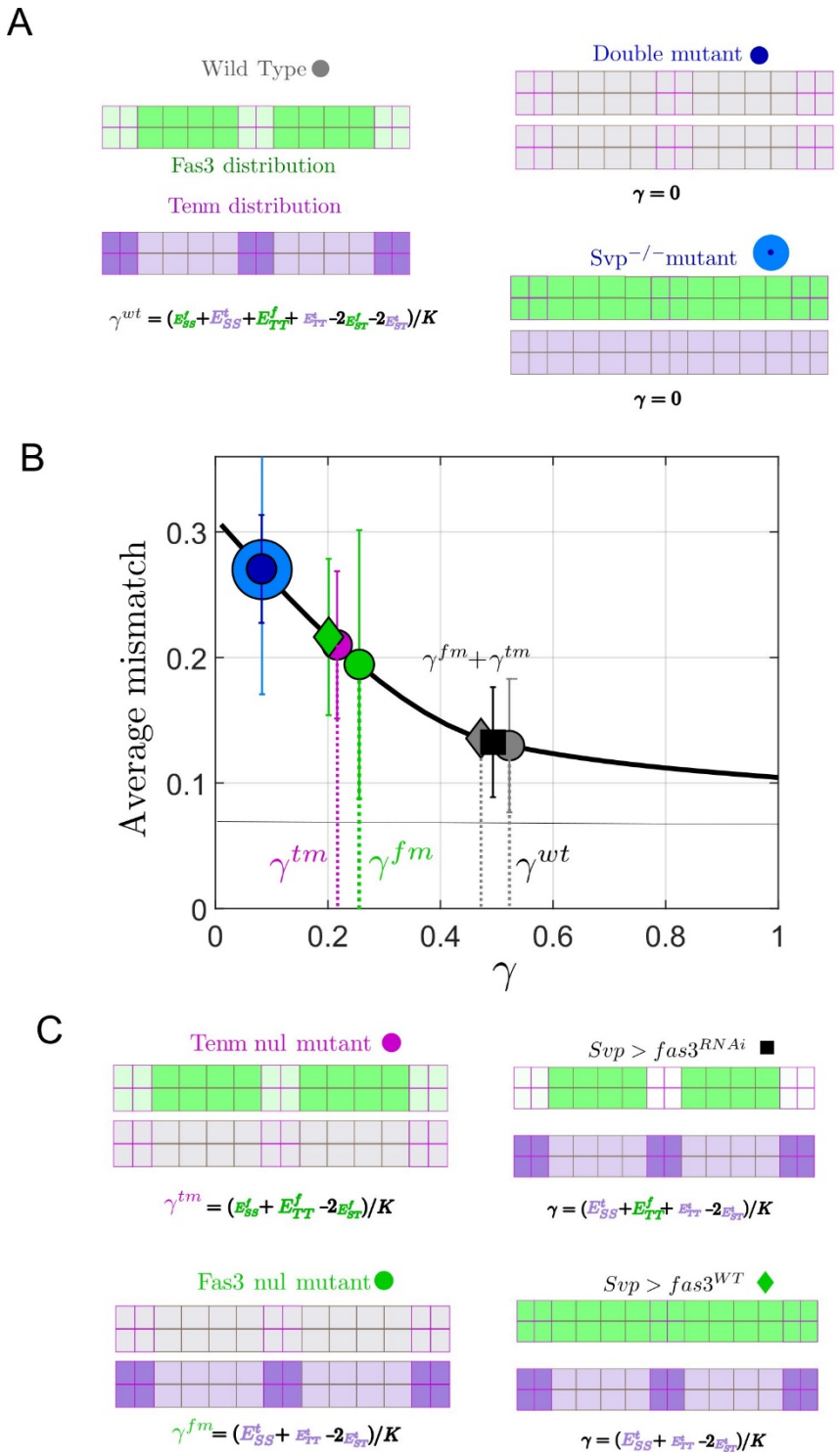

Figure 4: **Equilibrium energy description replicates experimental observations in wild type and mutants.** (A,B,C) Distribution of Fas3 (green) and Ten-m (purple) in wildtype and mutant embryos. The value of γ for wild type (grey circle), double mutant (blue small circle), *svp*$^{-/-}$ mutant (blue circle), *fas3*$^{-/-}$ (green circle) , *ten-m*$^{-/-}$ (purple circle), Svp-Gal4, Fas3-UAS (green diamond) and Svp-Gal4 > Fas3-RNAi-UAS (black square) embryos can be inferred from the average mismatch curve.

225 **Energy scales are just sufficient to ensure robust matching**

226

227 Perturbing the expression profiles of Fas3 and Ten-m, results in altering of the cardioblast cell
228 matching[32]. We next ask whether the model can reproduce these observations. To that end, we
229 use Figure 3E to estimate γ for wild type and mutants conditions (Figure 4A-C) given the
230 experimentally measured cell mismatch. We do not know the specific effective energy levels
231 associated with different adhesion interactions. To relate the values of $\epsilon_{TT}, \epsilon_{SS}$ and ϵ_{ST} to the
232 underlying dynamics, we assume that they depend on the energy scales of homophilic
233 interactions of Fas3 (ϵ_{aa}^{Fas3}) and Ten-m (ϵ_{aa}^{Ten}), *e.g.* $\epsilon_{TT} \approx \epsilon_{TT}^{Fas3} + \epsilon_{TT}^{Ten}$.

234

235 Our model predicts that mutants erasing the differential pattern of expression of Fas3 and Ten-
236 m lead to γ = 0 μm and a mismatch equal to the random case. This is the case for the double
237 mutant of *Fas3*$^{-/-}$ and *Ten-m*$^{-/-}$ and the mutant *svp*$^{-/-}$ (Figure 4A,B). For the wild type, we find
238 γ_{WT} ~ 0.5 μm which is smaller than the value γ_{WT} ~ 1 μm found by fitting the experimentally
239 measured spatial variation of mismatch (Figure 3G). However, this difference could be
240 explained by the shallowness of the mismatch curve for γ > 0.5 μm. Assuming that there is no
241 interaction between Fas3 and Ten-m, we expect that $\gamma_{WT} = \gamma_{Fas3} + \gamma_{Tenm}$. Using the
242 measured matching in mutants of Fas3 *Fas3*$^{-/-}$ and Ten-m *Ten-m*$^{-/-}$, we estimate the
243 contributions to γ_{WT} from the different adhesion molecules, and find $\gamma_{Fas3} + \gamma_{Tenm} \sim \gamma_{WT}$ ~0.5
244 μm (Figure 4B).

245

246 Our simple additive model of energies is consistent with other mutant observations. When Fas3
247 is overexpressed in Svp cells using Svp-Gal4, Fas3-UAS expressing embryos, we expect γ to
248 be the same than for the mutant *Fas3*$^{-/-}$, which is the case (Figure 4B-C). When the level of
249 Fas3 in Svp-positive cells is reduced using embryos expressing Svp-Gal4 > Fas3-RNAi-UAS,
250 ϵ_{SS} is reduced compared to wildtype, but so is ϵ_{ST} as direct interactions between filopodia with
251 Fas3 is reduced between different cell types. We find a γ similar to the wild-type case showing
252 that ϵ_{ST} is small compared to ϵ_{SS} and ϵ_{TT}.

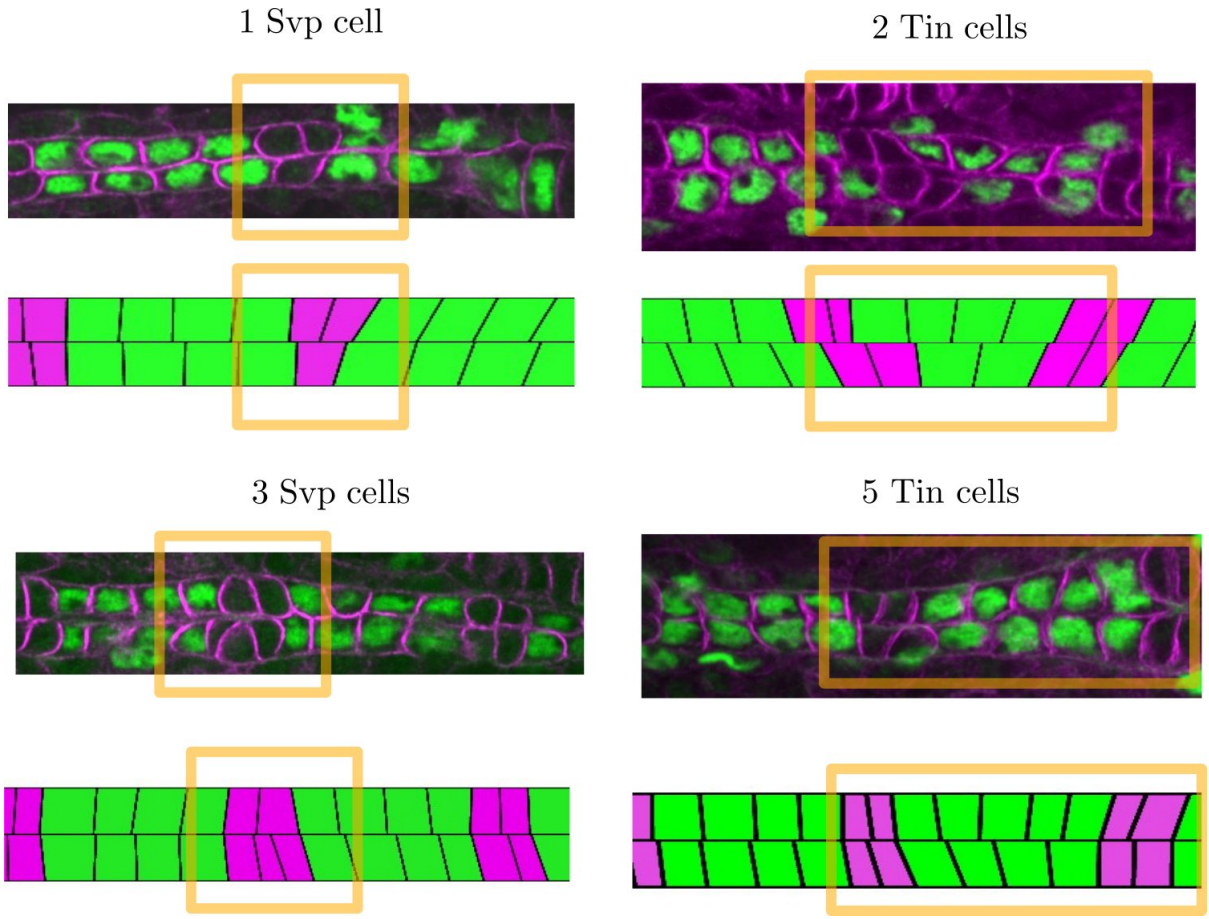

Figure 5: **Matching correction of local defects.** Various types of experimentally observed cell number defects in wild type embryonic hearts. Differential adhesion can partially compensate these defects by deforming cells in the range of $\gamma \approx 0.5$ found in Fig.4.

Robustness of cell matching to perturbations

Here, we probe the robustness of the system to perturbations in cell number by considering variations in cell type specification. Within wildtype embryo populations, we observe variability in the spatial pattern of cardioblast specification. For example, we have observed embryos with three and five Tin-positive cardioblasts in a sector, as well as a solitary Svp-positive cardioblast, and an additional one (Figure 5). Even when cell number is perturbed, we observe that the boundaries between different cell types are typically well defined. To test the model, we implemented different initial patterns of cardioblasts but otherwise kept parameters identical to the wildtype scenario with $\gamma = 0.5\ \mu m$. The system equilibrates to a state with clear boundaries between the different cell types and cells deform to align boundaries. This demonstrates that having two complementary adhesion processes is robust to perturbations in the structure of the heart as it develops.

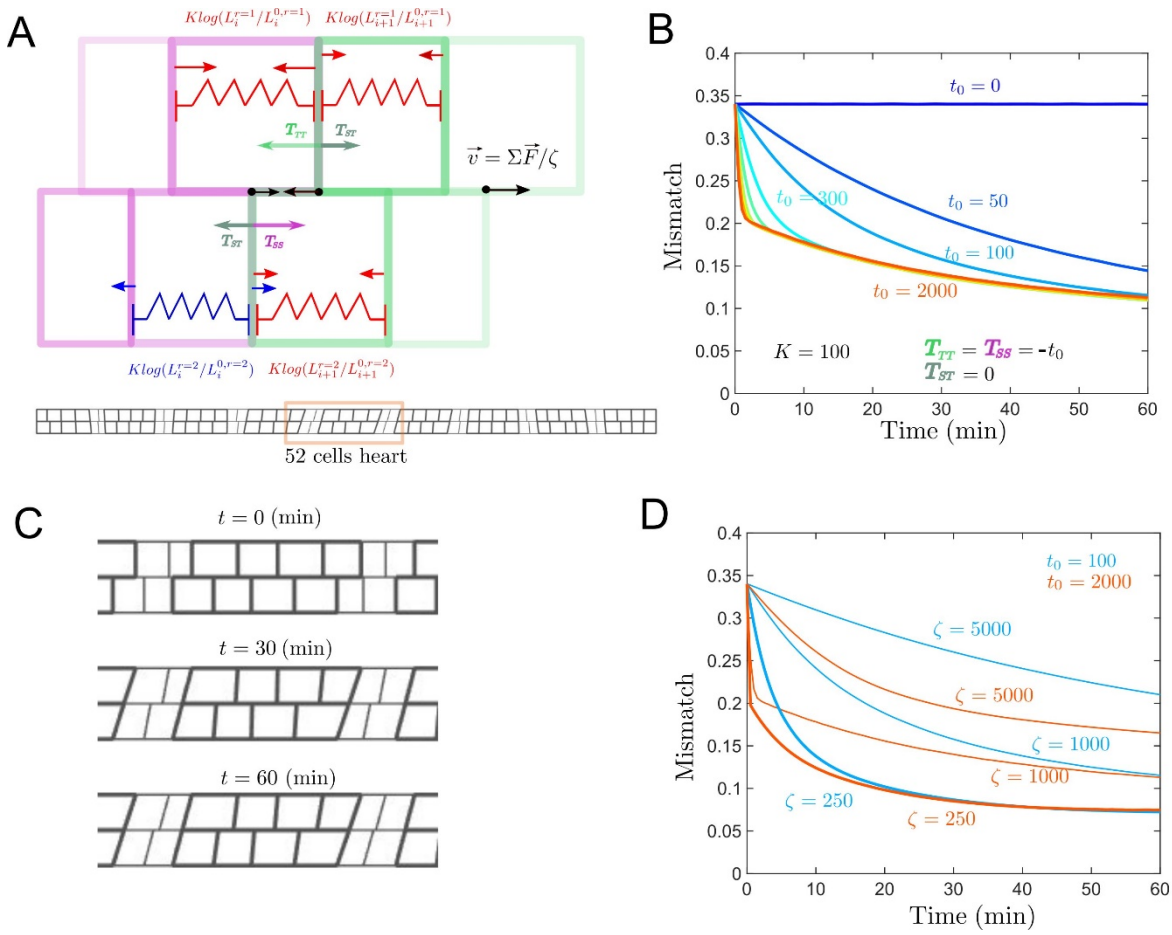

Figure 6: **Simulating cell matching dynamics** (A) Vertex model implementation of interface dynamics. Each cell-cell lateral boundary on a row is defined by a vertex point. Elastic forces are represented in red/blue depending if cells are stretched/compressed. Each cell-cell interface section between the two facing rows has a negative tension which acts on the vertices applying forces represented in magenta/green/grey depending on the interface type. The sum of these contributions divided by a friction coefficient, ξ, gives the vertex velocity. (B) We evolve the system (Methods) and compute the ensemble averaged mismatch over time (N = 30). We vary the tension t_0 between 0 and 2000 while K is fixed to 100 and ξ = 1000. (C) Spatial alignment for 0 min, 30 min, 60 min for $t_0 = 2000$, K= 100 and ξ = 1000 (D) Adhesion-independent cell alignment between cells of the same type depends on the friction coefficient ξ. Results shown for two different tensions, t_0.

Dynamic vertex model of cell matching

To evaluate how differential adhesion modulates cell matching dynamics, we used a vertex approach to model the time evolution of vertices at the interface between the two facing rows of cells, Figure 6A (see Methods). By analogy with the equilibrium energy model used previously, vertices are submitted to elastic forces corresponding to effective elasticity and

290 adhesion forces in the cell. We assume that adhesion produces a negative tension, which
291 extends cell-cell contact interfaces. The sum of these contributions results in a force which,
292 when divided by an effective friction coefficient, gives the vertex velocity. We explore the
293 simple case of equal tensions, $T_{\mathrm{SS}} = T_{\mathrm{TT}} = -t_0$ and $T_{\mathrm{ST}} = 0$ with a fixed K and friction
294 coefficient, ξ. Varying t_0, keeping other parameters fixed, shows a lower limit to cell matching
295 accuracy, as the time evolution of cell matching collapses onto a single curve for large t_0,
296 Figure 6B. This limit is consistent with our equilibrium model. At high adhesion differences,
297 the cell mismatch first undergoes a rapid decrease, which is adhesion-dependent. This
298 corresponds to the phase of heterogeneous cell types boundaries shrinking. Below a mismatch
299 of ~0.2, the boundaries between cell types are perfectly aligned, Figure 6C. The mismatch
300 between cells of the same type decreases with slower, adhesion independent, dynamics that are
301 friction dependent, Figure 6D. Overall, we see that dynamically incorporating differential
302 adhesion gives similar results to our equilibrium approach, supporting our above assumptions.
303
304 **Discussion**
305
306 Even though biological systems are inherently out-of-equilibrium, we have demonstrated that
307 an equilibrium energy argument is consistent with experimental observation of cell matching
308 in the heart. This is consistent with the rapid dynamics of filopodia compared to the time of
309 heart cells final alignment. The filopodia dynamics relate to the system effective temperature.
310 The idea of effective temperatures in developing systems has also recently been used to
311 describe jamming transitions during zebrafish development[36]. Our model shows that cell
312 matching results from the interplay between cell-cell interactions (mediated by filopodia and
313 specific adhesion molecules) and cell deformability. According to our model, the level of
314 differential adhesion found in the wildtype heart is close to the minimal level required to obtain
315 a well-aligned heart as the value $\gamma = 0.5$ corresponds to the point where the mismatch curve in
316 function of γ starts to flatten. We find that Fas3 and Ten-m contribute almost equally to the
317 matching process. Furthermore, we demonstrate than increasing differential adhesion
318 indefinitely does not accelerate the matching process beyond a certain point as the final
319 alignment phase is adhesion independent.
320
321 A key result of our model is that short-ranged constraints (*i.e.* adhesion differences between
322 two cell types) can propagate long-ranged order. We show that generating periodic segments

of different adhesion molecules (i) aligns these segments at their interfaces and (ii) alignment inside each segment is due to geometric confinement and decreases with the segment size.

Our work has potential application to other biological systems. During neurogenesis - where precise connections between neurons are required - Notch signalling (involve in lateral inhibition) has recently been shown to regulate neuronal wiring[10]. Formation of the vasculature requires cell migration to precise locations and this is mediated by filopodia protrusions and lateral inhibition[37]. During wound healing, cells need to repair wounds by forming precise connections. However, how processes at a single cell level are integrated to ensure long-ranged precise cell matching remains an open question[38]. In our model, we do not consider heterogeneities in the mechanical properties. In other systems such as the brain, tuning of tissue stiffness ensures precise cell matching[39]. More generally, coordinated cell migration can be directed by tissue stiffening[40]. It would be possible to test the role of mechanical feedback in our model by adding viscoelastic relaxation of the cell lengths within a vertex model framework as described in Figure 6.

Author Contributions

S.T. and T.E.S. designed the project with input from S.Z. S.T. and M.S. performed the simulations and modelling. S.Z. provided all experimental data. S.T. and T.E.S. wrote the manuscript, with contributions from M.S. and S.Z..

Acknowledgements

This work was supported by a Singapore Ministry of Education Academic Research Fund Tier 2 grant (MOE2018-T2-2-135), a Singapore National Research Foundation Fellowship (NRF2012NRF-NRFF001-094) and HFSP Young Investigator Grant (RGY0083/2016), all awarded to TES. Tinman antibody was a gift from Manfred Frasch.

Methods

Experiments

Experimental data collected as described in Zhang *et al.* [32].

Modelling

One-dimensional interface, and mismatch ratio definitions

The model system consists of two rows of equal number of cells interacting on a one-dimensional interface defined as vertices x. Each cell i on a row r is represented by a pair of vertices $(x_i^{(r)}, x_{i+1}^{(r)})$ on this interface with $x_i^{(r)} \leq x_{i+1}^{(r)}$ ($\mathrm{i} = 1, 2, \ldots, \mathrm{N}+1$, and $\mathrm{r} \in \{1, 2\}$ for N cells occupying each row), with cell length

$$L_i^{(r)} = x_{i+1}^{(r)} - x_i^{(r)}. \tag{SE1}$$

The total length of a model system is kept constant by fixing first $x_1^{(1)} = x_1^{(2)}$, and last $x_{N+1}^{(1)} = x_{N+1}^{(2)}$ vertices throughout the simulation. The overlap interval length between cells i and j located on two different rows is calculated as:

$$L(i \cap j) = \begin{cases} 0\,, \text{ if } \max\left(x_i^{(1)}, x_j^{(2)}\right) > \min\left(x_{i+1}^{(1)}, x_{j+1}^{(2)}\right) \\ \min\left(x_{i+1}^{(1)}, x_{j+1}^{(2)}\right) - \max\left(x_i^{(1)}, x_j^{(2)}\right), \ \ otherwise. \end{cases} \tag{SE2}$$

The mismatch ratio $m_i^{(r)}$ of a cell i on a row r is defined as a proportion of length of overlap with cells other than its sister cell i', and the total cell length of i:

$$m_i^{(r)} = \frac{L_i^{(r)} - L(i \cap i')}{L_i^{(r)}};\ m_i^{(r)} \in [0,1], \tag{SE3}$$

where the sister cell is defined as a cell i' with same index as i but located on a different row (i.e. $i' = i$), an average mismatch ratio of two sister cells is then calculated as $(m_i^{(1)} + m_{i'}^{(2)})/2$.

Calculating net change in energy

All vertices $x_i^{(r)}$ are assumed to be coupled with harmonic springs, with each cell having an elastic energy $\mathrm{E}_{\mathrm{el,i}}^{(\mathrm{r})} = \mathrm{K} \cdot \left(L_i^{(r)} - \mathrm{L}_{0,\mathrm{i}}^{(\mathrm{r})}\right)^2$, where $\mathrm{L}_{0,\mathrm{i}}^{(\mathrm{r})}$ is the equilibrium length for a given cell (kept constant throughout the simulation), and K is a spring constant. Then, the total elastic energy for the whole system is just a sum of elastic energies over all cells:

$$\mathrm{E_{el,total}} = \sum_{r=1}^{2}\sum_{i=1}^{N} \mathrm{K} \cdot \left(L_i^{(r)} - \mathrm{L}_{0,i}^{(r)}\right)^2. \quad \text{(SE4)}$$

In the model, two rows of cells interact along the one-dimensional interface by adhesion of cells along segments of the interface shared by the same cell type cells, or by cohesion of cells of two different cell types along interface segments occupied by cells of two different types. We implemented the interface by defining interface vertices $x_j^{(int)}$ with $x_j^{(int)} \leq x_{j+1}^{(int)}$, which could be obtained by concatenating both rows of $x_i^{(r)}$ vertices into single vector and then sorting them. Similar to cell vertices ($x_i^{(r)}$), pair of interface vertices ($x_j^{(int)}, x_{j+1}^{(int)}$) represents an interface segment j. The total adhesion energy for the whole system is then the sum of adhesion energy contributions of all interface segments:

$$E_{adh,total} = \sum_{j=1}^{2N+1} \epsilon_j \cdot (x_{j+1}^{(int)} - x_j^{(int)}), \quad \text{(SE5)}$$

where ϵ_j is the cell type specific adhesion energy-per-unit length of a segment j:

$$\epsilon_j = \begin{cases} \epsilon_{aa}, & j \text{ is interface between type } a \text{ and } a \\ \epsilon_{bb}, & j \text{ is interface between type } b \text{ and } b \\ \epsilon_{ab}, & j \text{ is interface between type } a \text{ and } b \end{cases} \quad \text{(SE6)}$$

Since vertices of $x_j^{(int)}$ are from both rows of cells, changing position of a single cell vertex $x_i^{(r)}$ could result in cases with $x_j^{(int)} \geq x_{j+1}^{(int)}$, thus $x_j^{(int)}$ needs to be sorted before calculating total adhesion energy during simulation.

The total energy of the system as a function of location of cell vertices $x_i^{(r)}$ is calculated as the sum of elastic and adhesive energies:

$$\mathrm{E}(x) = \mathrm{E_{el,total}} + E_{adh,total} \quad \text{(SE7)}$$

and the nett change in total energy due to change in the configuration of $x \to x + \Delta x$ is calculated as a difference in total energy between the two configurations

$$\Delta\mathrm{E}_{x \to x+\Delta x} = \mathrm{E}(x + \Delta x) - \mathrm{E}(x) \quad \text{(SE8)}$$

Sampling initial configuration and equilibrium lengths of cells

Randomness in cell shape geometry was modelled as a random initial configuration of cells, which was set to be equal to the equilibrium lengths of the cells throughout the simulation. The random initial configuration of cells, and thus the equilibrium lengths ($\mathrm{L}_{0,i}^{(r)}$) for each cell were sampled from a normal distribution with cell type specific mean and standard deviation using a MATLAB function *normrnd*. In order to construct a random configuration, we implemented random sequential deposition[41] of two rows onto each other with a constraint that enforces

equal length of two rows within $\varepsilon = \mu \cdot 10^{-3}$, where μ is the smallest of the two type-specific average lengths of the cells in the given configuration.

For the row of cells with $\mathrm{m_a}$ type a cells and $\mathrm{N} - \mathrm{m_a}$ type b cells, $\mathrm{m_a}$ equilibrium lengths ($\mathrm{L}_{0,\mathrm{i}}^{(1)}$) for the top row are sampled from a normal distribution with mean $L_{0,a}^{mean}$ and standard deviation $L_{0,a}^{std}$, and $\mathrm{N} - \mathrm{m_a}$ equilibrium lengths ($\mathrm{L}_{0,\mathrm{i}}^{(1)}$) are sampled from normal distribution with mean $L_{0,b}^{mean}$ and standard deviation $L_{0,b}^{std}$.

$$\mathrm{L}_{0,\mathrm{i}}^{(1)} \sim \begin{cases} \mathcal{N}\left(\mu = L_{0,a}^{mean}, \sigma = L_{0,a}^{std}\right) \text{ for type a} \\ \mathcal{N}\left(\mu = L_{0,b}^{mean}, \sigma = L_{0,b}^{std}\right) \text{ for type b} \end{cases}$$

where the mean and standard deviation for different cell types are experimentally determined parameters. Next, the bottom row equilibrium lengths ($\mathrm{L}_{0,\mathrm{i}}^{(2)}$) were sampled in the same manner until the constraint $\sum_{\mathrm{i}} \mathrm{L}_{0,\mathrm{i}}^{(1)} - \varepsilon < \sum_{\mathrm{i}} \mathrm{L}_{0,\mathrm{i}}^{(2)} < \sum_{\mathrm{i}} \mathrm{L}_{0,\mathrm{i}}^{(1)} + \varepsilon$ was satisfied. Afterwards, $\mathrm{L}_{0,\mathrm{i}}^{(\mathrm{r})}$ are converted into cell vertices $x_i^{(r)}$ in the same sequence as the $\mathrm{L}_{0,\mathrm{i}}^{(\mathrm{r})}$ was produced by *normrnd* function.

Implementation of Markov-chain cell configuration sampling using Metropolis algorithm

In order to simulate evolution of the cell boundaries by moving cell vertices x and sample cell configurations, we used Monte Carlo Markov-chain (MCMC) sampling by implementing Metropolis algorithm in MATLAB[42]. At each MCMC sampling step a vertex $x_i^{(r)}$ is selected randomly and a random move is proposed $x_i^{(r)} \to x_i^{(r)} + \Delta x_i^{(r)}$, $\Delta x_i^{(r)}$ is a Gaussian random variable with mean 0 and standard deviation δX, the value of δX determines magnitude of the random movement (interpreted as random fluctuations in the model). In our implementation $\Delta x_i^{(r)}$ was sampled using *normrnd(0, δX)* function in MATLAB. Afterwards, Metropolis probability of accepting the proposed move, $p(x_i^{(r)} \to x_i^{(r)} + \Delta x_i^{(r)})$ is calculated using

$$p(x_i^{(r)} \to x_i^{(r)} + \Delta x_i^{(r)}) = \min\left(1, exp\left(-\frac{\Delta \mathrm{E}_{x_i^{(r)} \to x_i^{(r)} + \Delta x_i^{(r)}}}{E_0}\right)\right) \quad \text{(SE9)}$$

where $\Delta \mathrm{E}_{x_i^{(r)} \to x_i^{(r)} + \Delta x_i^{(r)}}$ is a nett change in total energy of the system due to movement of vertex $x_i^{(r)}$ by amount $\Delta x_i^{(r)}$, and E_0 is the effective temperature ("thermal energy") of the cells. Then, $p(x_i^{(r)} \to x_i^{(r)} + \Delta x_i^{(r)})$ is compared to a uniformly distributed random variable δ_p in the

interval $\delta_p \in (0,1)$ produced by *rand* function in MATLAB. If the statement $\delta_p < p\left(x_i^{(r)} \to x_i^{(r)} + \Delta x_i^{(r)}\right)$ is true, then the move is accepted, and otherwise the move is rejected.

Overall, the probability of movement $x_i^{(r)} \to x_i^{(r)} + \Delta x_i^{(r)}$ of a vertex at position $x_i^{(r)}$ is:

$$P(x_i^{(r)} \to x_i^{(r)} + \Delta x_i^{(r)}) = \frac{1}{2 \cdot (N-1)} \cdot p(x_i^{(r)} \to x_i^{(r)} + \Delta x_i^{(r)})$$

where the first term on the right-hand-side refers to the probability of selecting vertex $x_i^{(r)}$ from two rows, and $N-1$ vertices in each row (two end vertices on each row are assumed to be fixed throughout the simulation, and have $P = 0$). In order to avoid flipping of cells, and overlapping of cells on a single row, we forbid such movements by setting $p\left(x_i^{(r)} \to x_i^{(r)} + \Delta x_i^{(r)}\right) = 0$ for movements with $\Delta x_i^{(r)} > 0$ that exceed cell length of cell i (i.e. $\Delta x_i^{(r)} > 0$ AND $\Delta x_i^{(r)} > L_i^{(r)}$), and for movements with $\Delta x_i^{(r)} < 0$ that exceed cell length of cell $i-1$ (i.e. $\Delta x_i^{(r)} < 0$ AND $|\Delta x_i^{(r)}| > L_{i-1}^{(r)}$).

Implementation of vertex model

Cell initial geometries are constructed using the same functions as with the equilibrium energy model above. Each vertex is described by its position $x_i^{(r)}(t)$,and follows the equation :

$\xi \frac{\partial x_i^{(r)}(t)}{\partial t} = (T_{adh}^{i+1} - T_{adh}^{i} + K * \log(L_{i+1}^{(r)}(t)/L_{i+1,0}^{(r)}) - K * \log(L_i^{(r)}(t)/L_{i,0}^{(r)})$ with $T_{adh} = T_{SS}$ for a S-S interface, $T_{adh} = T_{TT}$ for a T-T interface, and $T_{adh} = T_{ST}$ for a S-T interface. Here we use the elastic force form $K * \log(L_i^{(r)}(t)/L_{i,0}^{(r)})$ instead of $K * (L_i^{(r)}(t) - L_{i,0}^{(r)})$ to avoid numerical artefacts at big cell deformation. These two definitions are the same for small cell deformations. Time is discretized in time steps dt = 0.01 min and the parameter ξ order of magnitude is tuned to observe the dynamics of the system evolution on the minute/hour timescale. Our previous equilibrium model predicts that matching will occur when $K \backsim T_{adh}$ and on the hour timescale when $T_{adh}/\xi \backsim 1\ \mu m\ /\ min$. In Figure 6, T_{adh} and K are expressed in pN and ξ in pN *min / μm. The vertices positions are calculated at each simulation step and allow to calculate the mismatch evolution in time.

460 **References**

461

462 1. Lecuit, T. & Le Goff, L. Orchestrating size and shape during morphogenesis. Nature
463 450, 189–192 (2007).
464 2. Heisenberg, C.-P. & Bellaiche, Y. Forces in Tissue Morphogenesis and Patterning.
465 Cell 153, 948–962 (2013).
466 3. Collinet, C., Rauzi, M., Lenne, P.-F. & Lecuit, T. Local and tissue-scale forces drive
467 oriented junction growth during tissue extension. Nat. Cell Biol. 17, 1247–1258
468 (2015).
469 4. Pinheiro, D. & Bellaiche, Y. Mechanical Force-Driven Adherens Junction Remodeling
470 and Epithelial Dynamics. Dev. Cell 47, 3–19 (2018).
471 5. Olivotto, I., Cecchi, F., Poggesi, C. & Yacoub, M. H. Developmental origins of
472 hypertrophic cardiomyopathy phenotypes: a unifying hypothesis. Nat. Rev. Cardiology
473 6, 317–321 (2009).
474 6. Som, P. M. & Naidich, T. P. Illustrated Review of the Embryology and Development
475 of the Facial Region, Part 1: Early Face and Lateral Nasal Cavities. AJNR Am. J.
476 Neuroradiol. 34, 2233–2240 (2013).
477 7. Dixon, M. J., Marazita, M. L., Beaty, T. H. & Murray, J. C. Cleft lip and palate:
478 understanding genetic and environmental influences. Nature 12, 167–178 (2011).
479 8. Clandinin, T. R. & Zipursky, S. L. Making connections in the fly visual system.
480 Neuron 35, 827–841 (2002).
481 9. Sanes, J. R. & Yamagata, M. Many Paths to Synaptic Specificity. Annu. Rev. Cell
482 Dev. Biol. 25, 161–195 (2009).
483 10. Pinto-Teixeira, F. et al. Development of Concurrent Retinotopic Maps in the Fly
484 Motion Detection Circuit. Cell 173, 485–498.e11 (2018).
485 11. Takeichi, M. The cadherin superfamily in neuronal connections and interactions. Nat.
486 Rev. Neurosci. 8, 11–20 (2006).
487 12. Hong, W., Mosca, T. J. & Luo, L. Teneurins instruct synaptic partner matching in an
488 olfactory map. Nature 484, 201–207 (2012).
489 13. Maness, P. F. & Schachner, M. Neural recognition molecules of the immunoglobulin
490 superfamily: signaling transducers of axon guidance and neuronal migration. Nat.
491 Neurosci. 10, 19–26 (2007).
492 14. Berns, D. S., DeNardo, L. A., Pederick, D. T. & Luo, L. Teneurin-3 controls
493 topographic circuit assembly in the hippocampus. Nature 554, 328–333 (2018).
494 15. Harada, T., Harada, C. & Parada, L. F. Molecular regulation of visual system
495 development: more than meets the eye. Genes & Development 21, 367–378 (2007).
496 16. Kumar, J. P. Building an ommatidium one cell at a time. Dev. Dyn. 241, 136–149
497 (2011).
498 17. Wartlick, O., Julicher, F. & Gonzalez-Gaitan, M. Growth control by a moving
499 morphogen gradient during Drosophila eye development. Development 141, 1884–
500 1893 (2014).
501 18. Olson, E. N. Gene Regulatory Networks in the Evolution and Development of the
502 Heart. Science 313, 1922–1927 (2006).
503 19. Hunter, G. L. et al. Coordinated control of Notch/Delta signalling and cell cycle
504 progression drives lateral inhibition-mediated tissue patterning. Development 143,
505 2305–2310 (2016).
506 20. Shaya, O. et al. Cell-Cell Contact Area Affects Notch Signaling and Notch-Dependent
507 Patterning. Dev. Cell 40, 505–511.e6 (2017).
508 21. Gibson, M. C., Patel, A. B., Nagpal, R. & Perrimon, N. The emergence of geometric
509 order in proliferating metazoan epithelia. Nature 442, 1038–1041 (2006).

22. Umetsu, D. et al. Local increases in mechanical tension shape compartment boundaries by biasing cell intercalations. Curr. Biol. 24, 1798–1805 (2014).
23. Hamant, O. et al. Developmental patterning by mechanical signals in Arabidopsis. Science 322, 1650–1655 (2008).
24. Taniguchi, K. et al. Chirality in planar cell shape contributes to left-right asymmetric epithelial morphogenesis. Science 333, 339–341 (2011).
25. Hervieux, N. et al. A Mechanical Feedback Restricts Sepal Growth and Shape in Arabidopsis. Curr. Biol. 26, 1–10 (2016).
26. Le Garrec, J.-F. et al. A predictive model of asymmetric morphogenesis from 3D reconstructions of mouse heart looping dynamics. eLife 6, 421 (2017).
27. Matejčić, M., Salbreux, G. & Norden, C. A non-cell-autonomous actin redistribution enables isotropic retinal growth. PLoS Biol. 16, e2006018–29 (2018).
28. Collier, J. R., Monk, N. A., Maini, P. K. & Lewis, J. H. Pattern formation by lateral inhibition with feedback: a mathematical model of delta-notch intercellular signalling. J. Theor. Biol. 183, 429–446 (1996).
29. Kim, S., Cassidy, J. J., Yang, B., Carthew, R. W. & Hilgenfeldt, S. Hexagonal Patterning of the Insect Compound Eye: Facet Area Variation, Defects, and Disorder. Biophys. J. 111, 2735–2746 (2016).
30. Bi, D., Lopez, J. H., Schwarz, J. M. & Manning, M. L. A density-independent rigidity transition in biological tissues. Nature Physics 11, 1074–1079 (2015).
31. Hayashi, T. & Carthew, R. W. Surface mechanics mediate pattern formation in the developing retina. Nature 431, 647–652 (2004).
32. Zhang, S., Amourda, C., Garfield, D. & Saunders, T. E. Selective Filopodia Adhesion Ensures Robust Cell Matching in the Drosophila Heart. Dev. Cell 46, 189–203.e4 (2018).
33. Bodmer, R., Heart, M. F.2010. Heart Development and Regeneration: Development and Aging of the Drosophila Heart. 47–84 (Academic Press, 2010).
34. Kuntz, S. G. & Eisen, M. B. Drosophila Embryogenesis Scales Uniformly across Temperature in Developmentally Diverse Species. PLoS Genet. 10, e1004293 (2014).
35. Chong, J., Amourda, C. & Saunders, T. E. Temporal development of *Drosophila* embryos is highly robust across a wide temperature range. J. R. Soc. Interface 15, 20180304–11 (2018).
36. Atia, L. et al. Geometric constraints during epithelial jamming. Nature Physics 14, 613-620 (2018)
37. Bentley, K., Mariggi, G., Gerhardt, H. & Bates, P. A. Tipping the Balance: Robustness of Tip Cell Selection, Migration and Fusion in Angiogenesis. PLoS Comput. Biol. 5, e1000549–19 (2009).
38. Sonnemann, K. J. & Bement, W. M. Wound Repair: Toward Understanding and Integration of Single-Cell and Multicellular Wound Responses. Annu. Rev. Cell Dev. Biol. 27, 237–263 (2011).
39. Koser, D. E. et al. Mechanosensing is critical for axon growth in the developing brain. Nat. Neurosci. 19, 1592–1598 (2016).
40. Barriga, E. H., Franze, K., Charras, G. & Mayor, R. Tissue stiffening coordinates morphogenesis by triggering collective cell migration in vivo. Nature 554, 523–527 (2018).
41. Krauth, W. Statistical mechanics: algorithms and computations. (Oxford University Press, 2006).
42. Metropolis, N., Rosenbluth, A. W., Rosenbluth, M. N., Teller, A. H. & Teller, E. Equation of State Calculations by Fast Computing Machines. J. Chem. Phys. 21, 1087–1092 (1953).